SPACE SCIENCES

Processing of methane and acetylene ices by galactic cosmic rays and implications to the color diversity of Kuiper Belt objects

Chaojiang Zhang[1,2]†, Cheng Zhu[1,2]†, Andrew M. Turner[1,2], Ivan O. Antonov[1,2], Adrien D. Garcia[3], Cornelia Meinert[3], Leslie A. Young[4], David C. Jewitt[5], Ralf I. Kaiser[1,2]*

Kuiper Belt objects exhibit a wider color range than any other solar system population. The origin of this color diversity is unknown, but likely the result of the prolonged irradiation of organic materials by galactic cosmic rays (GCRs). Here, we combine ultrahigh-vacuum irradiation experiments with comprehensive spectroscopic analyses to examine the color evolution during GCR processing methane and acetylene under Kuiper Belt conditions. This study replicates the colors of a population of Kuiper Belt objects such as Makemake, Orcus, and Salacia. Aromatic structural units carrying up to three rings as in phenanthrene ($C_{14}H_{10}$), phenalene (C_9H_{10}), and acenaphthylene ($C_{12}H_8$), of which some carry structural motives of DNA and RNA connected via unsaturated linkers, were found to play a key role in producing the reddish colors. These studies demonstrate the level of molecular complexity synthesized of GCR processing hydrocarbon and hint at the role played by irradiated ice in the early production of biological precursor molecules.

INTRODUCTION

The Kuiper Belt (*1*) is a vast region beyond the orbit of Neptune occupied by ice-rich bodies. Dynamical and physical observations, including spectra that show volatiles including methane (CH_4), ammonia (NH_3), water (H_2O), and methanol (CH_3OH), have transformed our understanding of the origin and evolution of the solar system (*2*–*4*). The Kuiper Belt represents a region of leftover debris from the early history of the solar system holding more than 100,000 Kuiper Belt objects [KBOs; also referred to as trans-Neptunian objects (TNOs)] of diameters exceeding 100 km (*5*–*8*). A majority of the measured KBOs are too faint to allow the telescopic acquisition of compositionally diagnostic spectra. Instead, the optical colors of KBOs are used both as a crude proxy for the composition and as a tool with which to compare objects of different sizes and dynamical classes. Color measurements have revealed highly diverse surface colors ranging from slightly more blue than sunlight to ultrared (*9*–*13*). An understanding of the origin of this color variety along with the spectroscopic and chemical evolution of the icy surfaces through interaction with ionizing radiation from the Sun and galactic cosmic rays (GCRs) is of vital importance to the planetary science and astrobiology communities. First, because molecules carry chromophores, i.e., the part of a molecule that absorbs in the visible spectrum responsible for its coloring, the low-temperature formation of carbon-, hydrogen-, oxygen-, and nitrogen-bearing (CHON) molecules in the optically active surface layers changes the reflection spectra of KBOs (*11*, *14*). Detailed knowledge of the synthetic routes to these molecules can therefore help to shed light on the complex chemistry of KBOs and provides a rigorous scientific background regarding how important classes of organic molecules might have been formed, some of which may serve as fundamental molecular building blocks for nucleobases having strong astrobiological relevance (*15*). Second, dynamical simulations reveal that KBOs are the main source of short-period comets such as 67P/Churyumov-Gerasimenko (*16*), which in turn are considered delivery systems of biologically important molecules to the early Earth. Because the processed ices of KBOs can harbor biologically important precursors such as amino acids (*17*) and carbohydrates (*18*), an understanding of the chemical evolution of KBO surfaces can lead to knowledge of the origin and formation routes of astrobiologically relevant molecules in our solar system and on Earth (*19*–*22*).

The origin of the diversity of KBO surface colors presents a persistent puzzle (*15*, *23*–*26*). Spectral slopes—a quantitative measure of the dependence of the reflectance on the wavelength—and surface colors are affected by the surface composition and ultimately by chromophores (*25*–*28*). A wide range of optical colors ranging from slightly blue to neutral and very red (all relative to the color of the Sun) have been observed on, e.g., Orcus and Sedna, respectively. The reddish surfaces are believed to be attributed to the presence of tholins—a term coined by Sagan describing refractory, polymer-like organics of unfamiliar composition generated through space weathering of carbo-containing ices (*29*–*31*). However, the variety of colors suggests a considerable diversity of hitherto unknown origin in the present-day surface composition of the KBOs. Two main points of view prevail. In one, the colors represent variations in the primordial composition, with the different colors reflecting the original location of condensation prior to being scattered (*32*). In the other, the diversity of colors has an evolutionary origin, arising from the modification of the surface by ionizing radiation (*23*, *24*, *33*–*36*). Naturally, intermediate explanations are possible, with colors influenced both by the initial compositions of the KBOs and by surface modification from energetic particle bombardment. The evolutionary models are supported by some

[1]Department of Chemistry, University of Hawaii at Mānoa, Honolulu, HI 96822, USA. [2]W.M. Keck Laboratory in Astrochemistry, University of Hawaii at Mānoa, Honolulu, HI 96822, USA. [3]Université Côte d'Azur, Institut de Chimie de Nice, UMR 7272 CNRS, Nice 06108, France. [4]Department of Space Studies, Southwest Research Institute, Boulder, CO 80302, USA. [5]Department of Earth and Space Sciences, University of California, Los Angeles, Los Angeles, CA 90095, USA.
*Corresponding author. Email: ralfk@hawaii.edu
†These authors contributed equally to this work.

laboratory experiments (*37*–*40*), which show that ice samples decrease in reflectivity for all wavelengths upon exposure to proxies of Solar Wind protons (*29*). The color differentiation has been suggested to be the result of processed methane ices on the colder objects leading to reddish objects, whereas on warmer KBOs with semi-major axes less than ~40 astronomical unit (AU), methane sublimates, making it unavailable to produce reddish colors (*41*–*44*). Visible near-infrared reflectance spectra of irradiated frozen methane revealed strong reddening and darkening of spectra after exposure to ionizing radiation at doses of up to 22 eV amu^{-1} (*45*). However, a systematic approach investigating the physical and chemical changes of ice compositions mimicking KBO surfaces is still lacking with spectral gradients, colors, and a detailed catalog of the molecular carriers and their chromophores formed in the irradiation processes being largely elusive as of now.

Here, we combine laboratory experiments with a complementary array of spectroscopic diagnostics to systematically explore the physical and chemical processes underlying the reddening of hydrocarbon-rich KBOs. Our objective is to provide an inventory of molecular carriers along with their controlling chromophores and apply these findings to constrain the cause of color diversity of those KBOs with hydrocarbon-dominated surfaces. Because the laboratory exposure time of KBO analog surfaces can be scaled to the corresponding time of exposure experienced by a KBO, this provides the potential to reconstruct the composition of hydrocarbon-rich surfaces of outer solar system bodies at the time of their formation billions of years ago and allows us to probe how the original state and chemical evolution affect the colors of KBOs (*44*–*49*). Methane is the simplest primordial hydrocarbon. It has been identified on the surfaces of large KBOs, including Pluto, Makemake, Eris, and Sedna (*50*, *51*), along with one of its radiolysis products, acetylene (C_2H_2). Note that water, methanol, and ammonia are also important constituents of surfaces of KBOs (*50*–*54*); sulfur also has been proposed (but not observed) as a contributor to KBO surface colors (*40*, *55*–*57*). However, it is not the goal of this study to prepare ice mixtures containing all five elements (C, H, N, O, and S) simultaneously; this approach would be futile in identifying the fundamental mechanisms leading to the KBO color variation and in deciphering the carriers of (groups of) chromophores responsible for the color variety across diverse populations of KBOs. It is the goal to start from simple ices (methane, acetylene) before moving to complex mixtures in future experiments. By focusing first on a population of KBOs with hydrocarbon-rich surfaces, only this step-by-step strategy will ultimately untangle the effect of the chemical composition of the KBO ices on the color feature of airless KBOs. Therefore, in our experiments, we exposed methane and acetylene ices to proxies of the GCR flux—with doses up to 80 eV amu^{-1} (table S1) at surface temperatures lower than 40 K; these

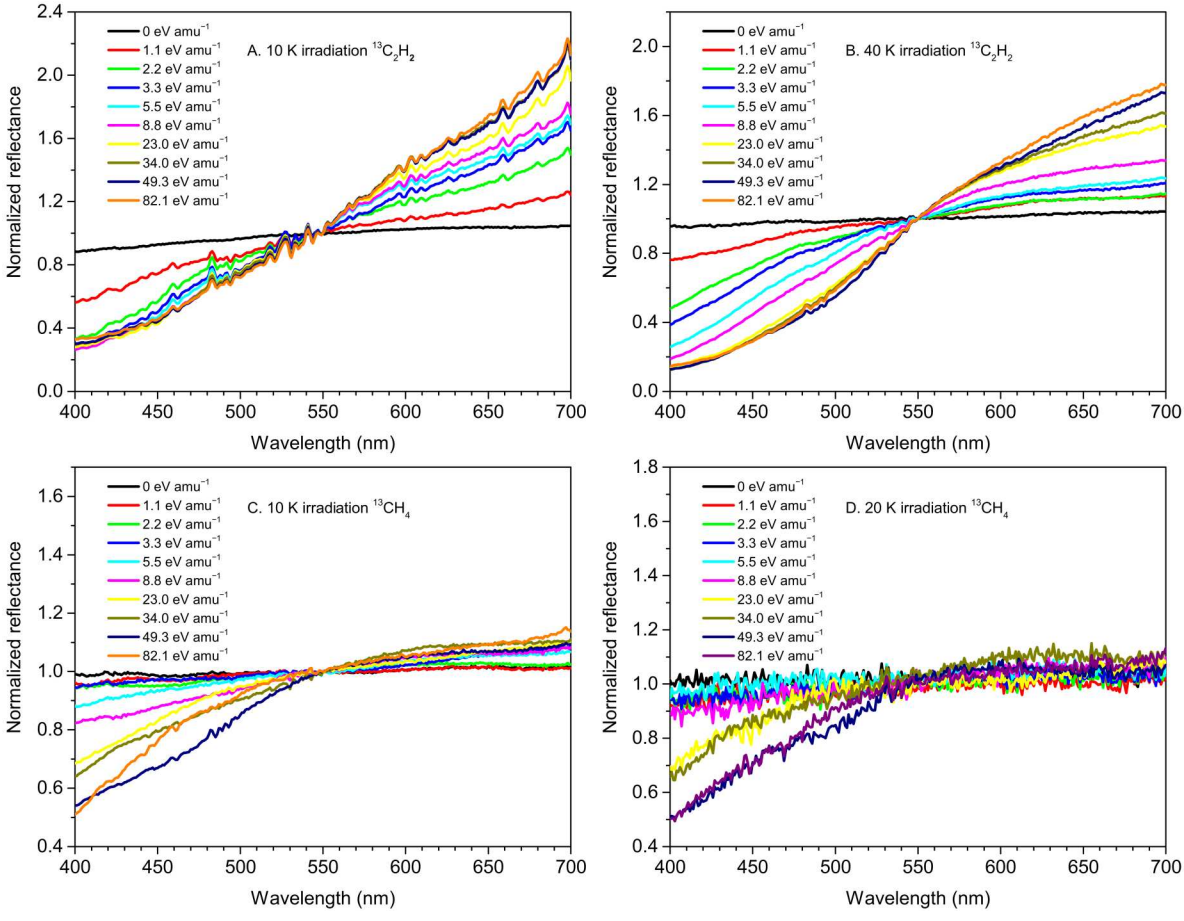

Fig. 1. UV-vis reflectance spectra collected during the irradiation of ^{13}C-acetylene ($^{13}C_2H_2$) and ^{13}C-methane ($^{13}CH_4$) ices. (**A**) $^{13}C_2H_2$ ice irradiated at 10 K. (**B**) $^{13}C_2H_2$ ice irradiated at 40 K. (**C**) $^{13}CH_4$ ice irradiated at 10 K. (**D**) $^{13}CH_4$ ice irradiated at 20 K. All the spectra were normalized at 550 nm.

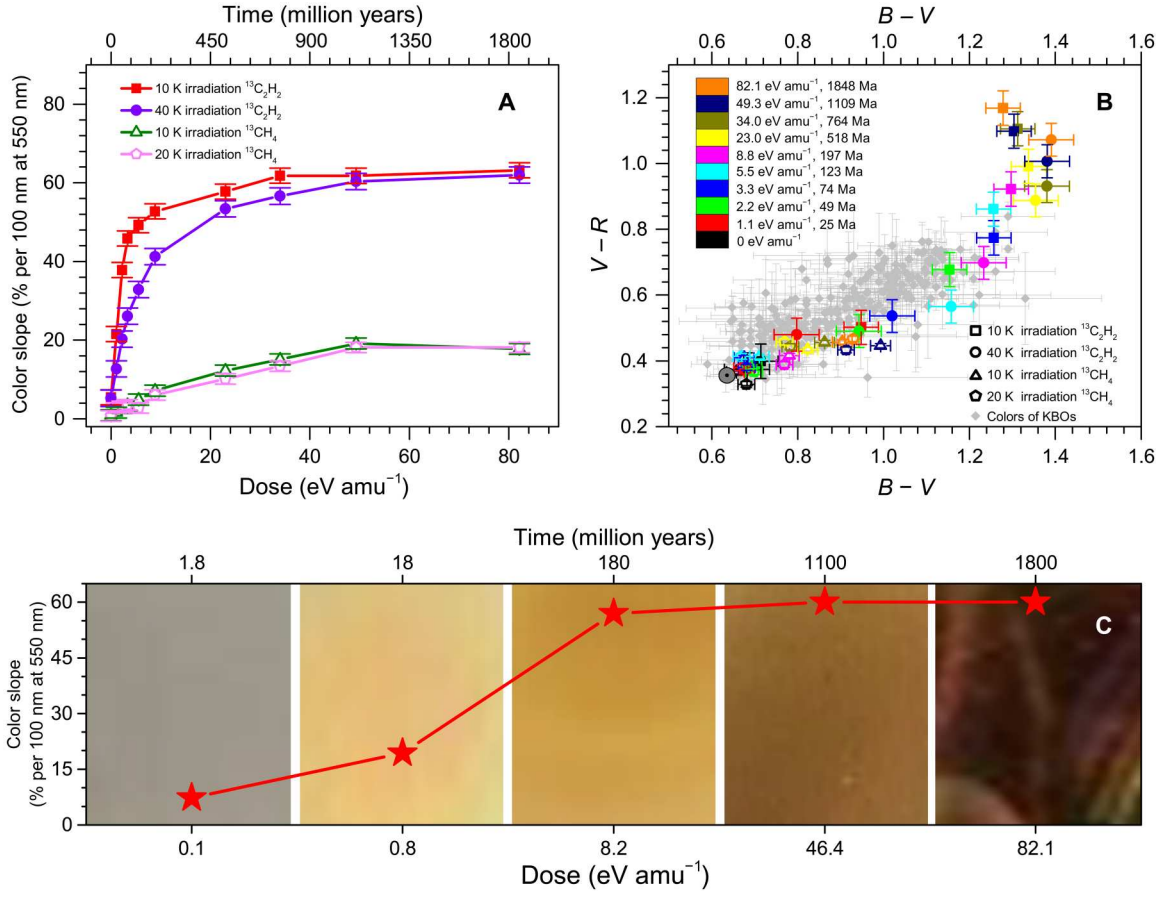

Fig. 2. Comparison of the color from irradiated ^{13}C-acetylene ($^{13}C_2H_2$) and ^{13}C-methane ($^{13}CH_4$) ices with KBOs. (**A**) Color slopes of irradiated ^{13}C-acetylene ($^{13}C_2H_2$) and ^{13}C-methane ($^{13}CH_4$). (**B**) Color-color diagram comparing irradiated ^{13}C-acetylene ($^{13}C_2H_2$) and ^{13}C-methane ($^{13}CH_4$) at different doses with KBOs. The colors of 10 K $^{13}C_2H_2$ (square), 40 K $^{13}C_2H_2$ (circle), 10 K $^{13}CH_4$ (triangle), and 20 K $^{13}CH_4$ (pentagon) are obtained from their UV-vis spectra. The gray circle indicates the color of the Sun. (**C**) Images of the residues for ^{13}C-acetylene ($^{13}C_2H_2$) ices irradiated at 10 K at distinct doses recorded after annealing the ices to 300 K.

doses simulate exposure times of hydrocarbons on KBO surfaces of about 1800 million years at 40 AU (*58*). Simultaneously, the evolution of functional groups associated with highly unsaturated hydrocarbons such as (polycyclic) aromatics and their precursors was quantified through Fourier transform infrared (FTIR) spectroscopy. Last, the soluble component of the organic residues was analyzed by two-dimensional gas chromatography time-of-flight mass spectrometry (GC×GC-TOF-MS), while the insoluble matter was characterized via time-of-flight secondary ion mass spectrometry (TOF-SIMS). Aromatic structural units carrying up to three rings as in phenanthrene ($C_{14}H_{10}$), phenalene (C_9H_{10}), and acenaphthylene ($C_{12}H_8$), of which some carry structural motives of nitrogen bases of DNA and RNA connected via unsaturated linkers, were found to play a key role in producing the reddish colors of KBOs such as Makemake, i.e., a population of KBOs located at distances from 39 to 44 AU from the Sun indicating effective exposure ages of the surfaces of at least 1100 million years. It further constrains for the first time the primordial surface composition of those KBOs with hydrocarbon surfaces, proposes processing times of KBO surfaces at temperatures lower than 40 K, and defines the level of molecular complexity of a population of KBOs with hydrocarbon surfaces synthesized in the prebiotic evolution of our solar system since the time of formation billions of years ago.

RESULTS

UV-vis spectroscopy—Slopes and colors

Ultraviolet-visible (UV-vis) spectroscopy provides an elegant methodology for tracing the change of spectral slopes and colors of the surfaces in situ during the radiation exposure of KBO model ices. Representative UV-vis reflectance spectra of irradiated methane ($^{13}CH_4$; 10 and 20 K) and acetylene ($^{13}C_2H_2$; 10 and 40 K) ices exposed to energetic electrons as proxies of GCRs (*59*, *60*) are presented in Fig. 1 (Materials and Methods). Note that aromatic molecules are widespread in the environment. Therefore, to eliminate any potential contaminants, pure ^{13}C-labeled reactants (^{13}C-methane and ^{13}C-acetylene, 99.9%) were used. This results in fully ^{13}C-labeled products such as aromatics, which are not present in the environment. Therefore, any fully ^{13}C-labeled molecule must be the result of the radiation processing of the ices. To compare our results with astronomical observations of KBOs (*61*, *62*), the visible range of the spectra (400 to 700 nm) was normalized with respect to the reflectance at 550 nm; color slopes S'—also referred to as spectral gradients—were calculated through a procedure defined in literature (*13*, *63*) (Fig. 2) exploiting Eq. 1 with the color slope S' (% per 100 nm) and reflectance R of the spectrum at the

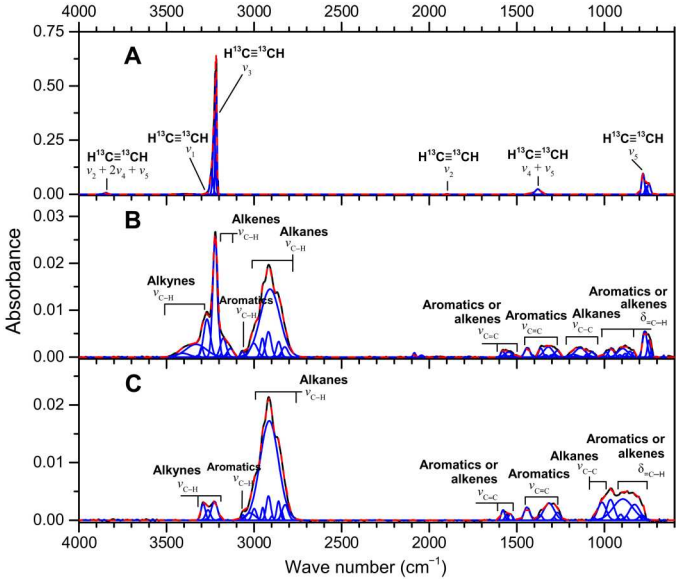

Fig. 3. Deconvoluted FTIR spectra of ^{13}C-acetylene ($^{13}C_2H_2$). (**A**) Pristine ices at 10 K. (**B**) After irradiation at 10 K. (**C**) Residue at 300 K. Assignments are compiled in table S2. FTIR spectra of irradiated ^{13}C-acetylene ($^{13}C_2H_2$) at 40 K, irradiated ^{13}C-methane ($^{13}CH_4$) at 10 K, and irradiated ^{13}C-methane ($^{13}CH_4$) at 20 K can be found in figs. S2 to S4, while peak assignments are listed in tables S3 to S5.

wavelength λ (nm)

$$S' = \frac{dR/d\lambda}{R_{550\mathrm{nm}}} \times 100\% \times 100\ \mathrm{nm} \quad (1)$$

Note that in astronomy, color is defined as the difference in magnitude of radiant flux (logarithmic scale) between two different filters. For the spectrum of an astronomical object, the color is determined via Eq. 2 in which $B - V$ is the color of the astronomical object through B and V filters, $(B - V)_{\mathrm{Sun}}$ is the reference color of the Sun, and Δλ is the difference between the central wavelengths of the B and V filters, with filter ranges of 390 to 510 nm (B) and 490 to 590 nm (V). To compare with astronomical observations, we also calculated the $V - R$ color through V and R filters with wavelength range of 490 to 590 nm (V) and 590 to 710 nm (R) (*13*, *63*, *64*)

$$B - V = (B - V)_{\mathrm{Sun}} + 2.51 \log\left(\frac{2 + S\Delta\lambda}{2 - S\Delta\lambda}\right) \quad (2)$$

Figure 1 shows that the UV-vis spectra of the pristine ices are approximately linear and flat, with S' ~ 0% per 100 nm. The slope increases as the radiation dose rises to nearly 50 eV amu^{-1}. This dose-dependent reddening effect is more pronounced for acetylene ices compared to methane ices with high-dose color slopes reaching S' ~ 60% versus S' ~ 20% per 100 nm, respectively (Fig. 2A). For acetylene ices, the color slopes rise faster for the 10 K ices compared to 40 K for doses close to 50 eV amu^{-1}; thereafter, the color slopes reach asymptotic values S' ~ 60% and 20% per 100 nm for acetylene and methane, respectively. The rising color-color trend exhibited by the KBOs (*61*, *62*) is well-matched by the irradiated ice data, as seen in Fig. 2B. First, irradiated methane ices can match the population of KBOs defined by $B - V$ ~ 0.7 to 1.2 and $V - R$ ~ 0.3 to 0.7, respectively. The overall trend in the irradiation data suggests that the $B - V$ and $V - R$ colors rise with increasing irradiation time, up to a KBO exposure age of about 1100 million years at 40 AU. In other words, exposed methane ice surfaces represent a fundamental constraint on KBO exposure times of up to nearly a billion years, perfectly delineating the lower bounds in $B - V$ versus $V - R$ color space. In contrast, the irradiated acetylene ices become redder than the KBOs for exposure ages exceeding 130 million years; irradiated acetylene ice can occupy only a fraction of the KBO surface to match the empirical colors.

Besides the slopes (Fig. 2A) and color-color diagrams (Fig. 2B), we also explored the optical colors of the organic residues formed after radiation exposure and annealing the ices to 300 K. This annealing phase mimics the transport of a KBO from the Kuiper Belt to the inner solar system as a short-period comet. Unexpectedly, the color slopes of the irradiated hydrocarbon systems are independent of the temperature (fig. S1). In the methane system, values of 17 ± 3% per 100 nm could be extracted and essentially reveal no temperature dependence. Likewise, the slopes for the acetylene system are within the error limits identical from 64 ± 6% to 59 ± 6% per 100 nm from 10 K to 300 K, respectively. This suggests that the surface colors of KBOs with dominant hydrocarbon complex organic molecules are temperature invariant during annealing up to 300 K, which is unlike the reddish coloration of methanol and water ice mixtures irradiated with nitrogen-containing cryoplasma at 85 K visually faded and disappeared at 120 to 150 K (*65*, *66*). Observations show that short-period comets and Centaurs (a dynamically intermediate phase between the Kuiper Belt and the comets) are depleted in ultrared ($S' \geq 25\%$ per 100 nm) matter at perihelion distances smaller than 8 to 10 AU, where blackbody temperatures are 90 to 100 K or higher (*14*). Hence, our laboratory result shows that this depletion cannot be attributed to the thermal instability of irradiation products formed in the Kuiper Belt. The optical colors strongly depend on the GCR dose and change from gray via yellowish to brown and nearly black as the radiation exposure increases to 82.1 eV amu^{-1} (Fig. 2C). Consequently, nonequilibrium radiation chemistry is fundamental to the ultimate surface colors of KBOs. Together, our simulation experiments reproduce the empirical color-color data for a population of airless KBOs covering $B - V$ = 0.7 to 1.3 and $V - R$ = 0.3 to 0.9, respectively, with the irradiation dose revealing a vital influence on the color and hence chemical evolution of the processed KBO surfaces. Additionally, the *New Horizons* mission revealed extensive colored terrains on Pluto's surface (*67*) comprising black to reddish regions such as Cthulhu Macula along Pluto's equator to yellowish topologies like Lowell Regio and Sputnik Planitia (*68*). Because photochemical models of Pluto's atmosphere reveal that acetylene represents a main hydrocarbon molecule precipitating on Pluto's surface (*69*, *70*) and the optical colors of the organic residues of irradiated acetylene at different doses in Fig. 1C reveal comparable colors of Pluto's surface, the reddish to black organic matter on Pluto likely originates from hydrocarbon products formed by the radiolysis of Pluto's surface hydrocarbons by energetic GCR. Note that, although the optical colors of the residues from irradiated acetylene well match Pluto's haze, the residues from irradiated ice containing nitrogen and oxygen also play an important role in Pluto's chemistry since these elements have been observed on its surface (*69*–*71*). However, laboratory studies exploiting simple hydrocarbon ices are required first before exposing complex mixtures containing all four elements (C, H, N, and O) to decipher the carrier of the (mixture) of chromophores responsible for the color of KBOs.

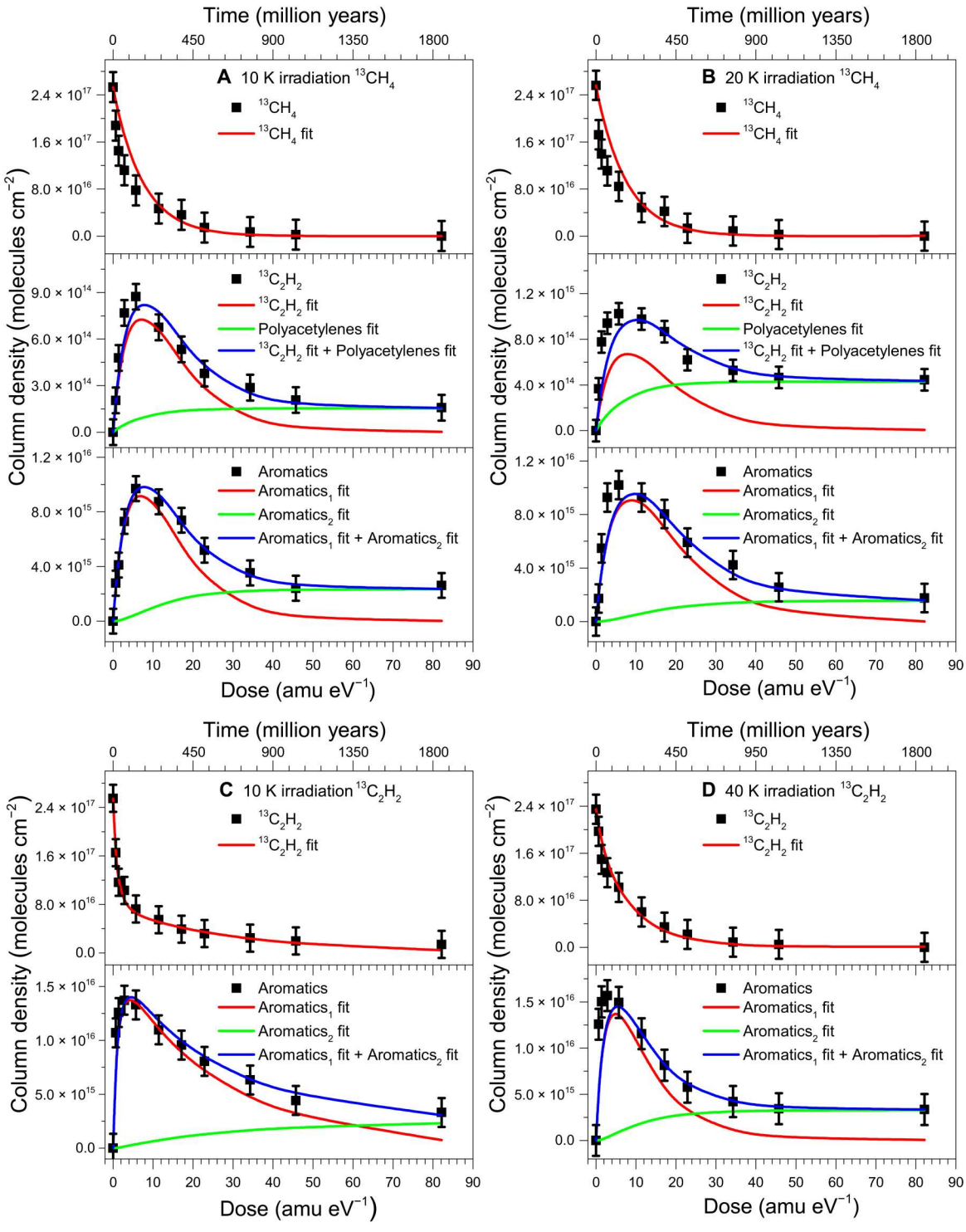

Fig. 4. Temporal evolution of key species for irradiated ^{13}C-acetylene ($^{13}C_2H_2$) and ^{13}C-methane ($^{13}CH_4$) along with its kinetic fits. (**A**) Integrated areas at 2999 cm^{-1} ($^{13}CH_4$), 3222 cm^{-1} ($^{13}C_2H_2$), and 3068 cm^{-1} (aromatic) for irradiated methane ($^{13}CH_4$) at 10 K. (**B**) Integrated areas at 2999 cm^{-1} ($^{13}CH_4$), 3222 cm^{-1} ($^{13}C_2H_2$), and 3068 cm^{-1} (aromatic) for irradiated methane ($^{13}CH_4$) at 20 K. (**C**) Integrated areas at 3222 cm^{-1} ($^{13}C_2H_2$) and 3070 cm^{-1} (aromatic) for irradiated acetylene ($^{13}C_2H_2$) at 10 K. (**D**) Integrated areas at 3222 cm^{-1} ($^{13}C_2H_2$) and 3070 cm^{-1} (aromatic) for irradiated acetylene ($^{13}C_2H_2$) at 40 K. Rate constants are compiled in table S6.

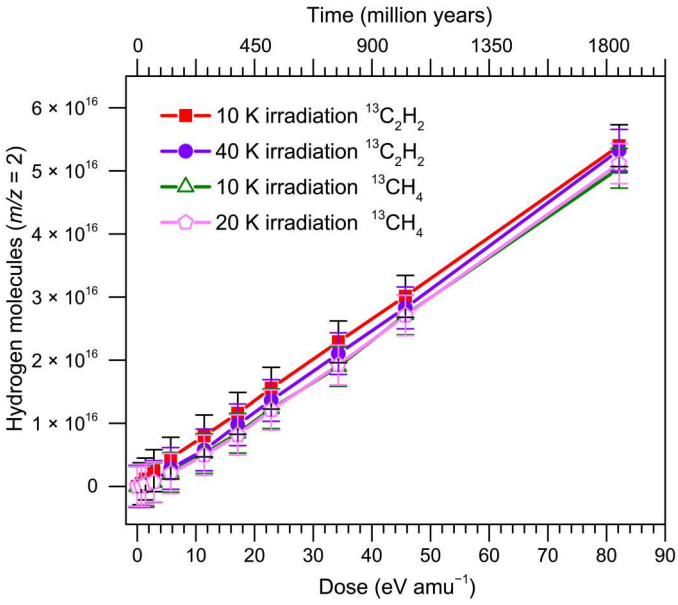

Fig. 5. Development of molecular hydrogen (H_2, m/z = 2) versus the dose during the irradiation of ^{13}C-acetylene ($^{13}C_2H_2$) and ^{13}C-methane ($^{13}CH_4$) ices.

Overall, the reddening of the KBO analog ices and of any organic material can plausibly be associated with increased delocalization of π electrons and a reduced excitation energy of the π → π* transition in aromatic molecules (*72*). However, it is not feasible to define specific chromophores from the reflection spectra alone due to their featureless slopes. Both polyacetylene (molecules carrying multiple conjugated —C≡C— moieties) and polycyclic aromatic hydrocarbons (PAHs; molecules carrying multiple fused benzene rings) along with their derivatives reveal strong electronic transitions from 400 to 800 nm and, hence, represent viable candidates (*73*). Therefore, complementary analytical techniques as described below are required to constrain the chromophores in the exposed hydrocarbon ices.

FTIR spectroscopy—Functional groups

FITR spectroscopy represents an ideal tool with which to identify functional groups in complex mixtures of organic molecules and to trace their evolution during radiation exposure to methane and acetylene ices. Representative spectra are provided in Fig. 3; a comprehensive set of FTIR data along with their assignments are compiled in figs. S2 to S4 and tables S2 to S5. First, the infrared spectrum of the pristine acetylene ice (Fig. 3A) shows prominent absorptions (*74*, *75*) such as the C—H stretching (3317 and 3216 cm^{-1}; ν_1 and ν_3) and C≡C—H bending modes (745 to 782 cm^{-1}; ν_5). After irradiation at 10 K (Fig. 3B), a series of new absorptions emerged. These could be linked to C—H stretching modes of alkynes (3374 to 529 cm^{-1}), alkenes (3128 to 3170 cm^{-1}), aromatics (3000 to 3070 cm^{-1}), and alkanes (2852 to 2952 cm^{-1}) (*76*, *77*). Weak features between 1022 and 1581 cm^{-1} can be assigned to carbon-carbon stretching modes of aromatics, alkenes, and alkanes, while absorptions from 833 to 989 cm^{-1} are attributed to C=C—H out-of-plane deformation modes of aromatics and/or alkenes (*76*). After annealing to 300 K, the infrared spectrum of the residues (Fig. 3C) reveals comparable absorption features save for the acetylene reactant. The infrared spectra of the acetylene ice after irradiation at 40 K and the corresponding residue at 300 K reveal qualitatively identical functional groups (fig. S2). Second, for the FTIR spectra of the irradiated methane ices at 10 K (fig. S3) and 20 K (fig. S4), multiple infrared bands were also detected (tables S4 and S5) (*78*). These absorptions correspond to the C—H stretching mode of alkynes (3263 and 3409 cm^{-1}) and alkenes (3149 and 3174 cm^{-1}); functional groups of aromatics such as the C—H stretching mode (3016 and 3065 cm^{-1}) were also detected. The newly emerging absorption bands of acetylene, for example, those at 3222 cm^{-1} in the exposed methane ices along with the fits as detailed below, suggest that methane can be effectively converted to acetylene at 10 and 20 K as suggested by a previous study (*78*).

Next, we explore the evolution of the absorptions as a function of the irradiation time (Fig. 4) and compare these results with the observed reddening from the UV-vis data to ultimately reveal potential molecular carriers causing the changing KBO surface colors. For methane (Fig. 4A), the C—H stretching mode (2999 cm^{-1}) decreases as the irradiation dose rises, thus documenting the destruction of pristine methane. Simultaneously, the integrated band areas of acetylene and aromatics monitored through their 3222 and 3068 cm^{-1} absorptions reveal a monotonous growth up to about 10 eV amu^{-1}, followed by a decrease to asymptotic values of about 20 to 30% compared to their peak abundances. These patterns imply essentially a consecutive kinetics scheme A (methane) → B (acetylene) → C (aromatics) → D (polymeric aromatics) converting methane to acetylene and then to aromatics. To fit the temporal profiles, this scheme had to be expanded by introducing a branched reaction from A (methane) to C (aromatics) and polyacetylenes. This conclusion is also supported by the conversion of acetylene to aromatics (Fig. 4C) as elucidated in the acetylene system. These patterns depict a reduction of the acetylene fundamentals with increasing dose. The aromatics constantly increase until about 10 eV amu^{-1}, then decrease in intensity, and eventually flatten off at about 25% of the peak intensity, hence also reinforcing an overall consecutive reaction mechanism A′ (acetylene) → B′ (aromatics) → C′ (polymeric aromatics), in which the first reaction step is reversible (Materials and Methods). The "earlier" peaking of the aromatics in the acetylene compared to the methane system can be rationalized that the acetylene reacts via A′ (acetylene) → B′ (aromatics) to the aromatics, whereas in the methane system, acetylene must first be produced, which delays the production of aromatics. It also results that the peak abundances of aromatics are about 40% lower in the methane system than in acetylene. It should be noted that even the very first step, i.e., the de facto conversion of two methane molecules into acetylene, formally produces three hydrogen molecules (Eq. 3). This conversion proceeds via ethane (C_2H_6) and ethylene (C_2H_4) (*79*, *80*). Furthermore, although the net production of benzene (C_6H_6) from acetylene does not release molecular hydrogen (Eq. 4) (*67*), subsequent molecular mass growth processes even to the simplest PAH naphthalene ($C_{10}H_8$) require the release of molecular hydrogen as depicted schematically in Eq. 5. In our experiments, the molecular hydrogen release was verified experimentally with the help of a quadrupole mass spectrometer (QMS; Materials and Methods). As the radiation dose increases, the efficiency of molecular hydrogen production increases for both the methane and the acetylene systems reaching up to 5.2 ± 0.2 × 10^{16} molecules (Fig. 5). Accounting for the infrared spectroscopically derived consumption of the methane and acetylene reactants, this accounts for only 4.3 ±

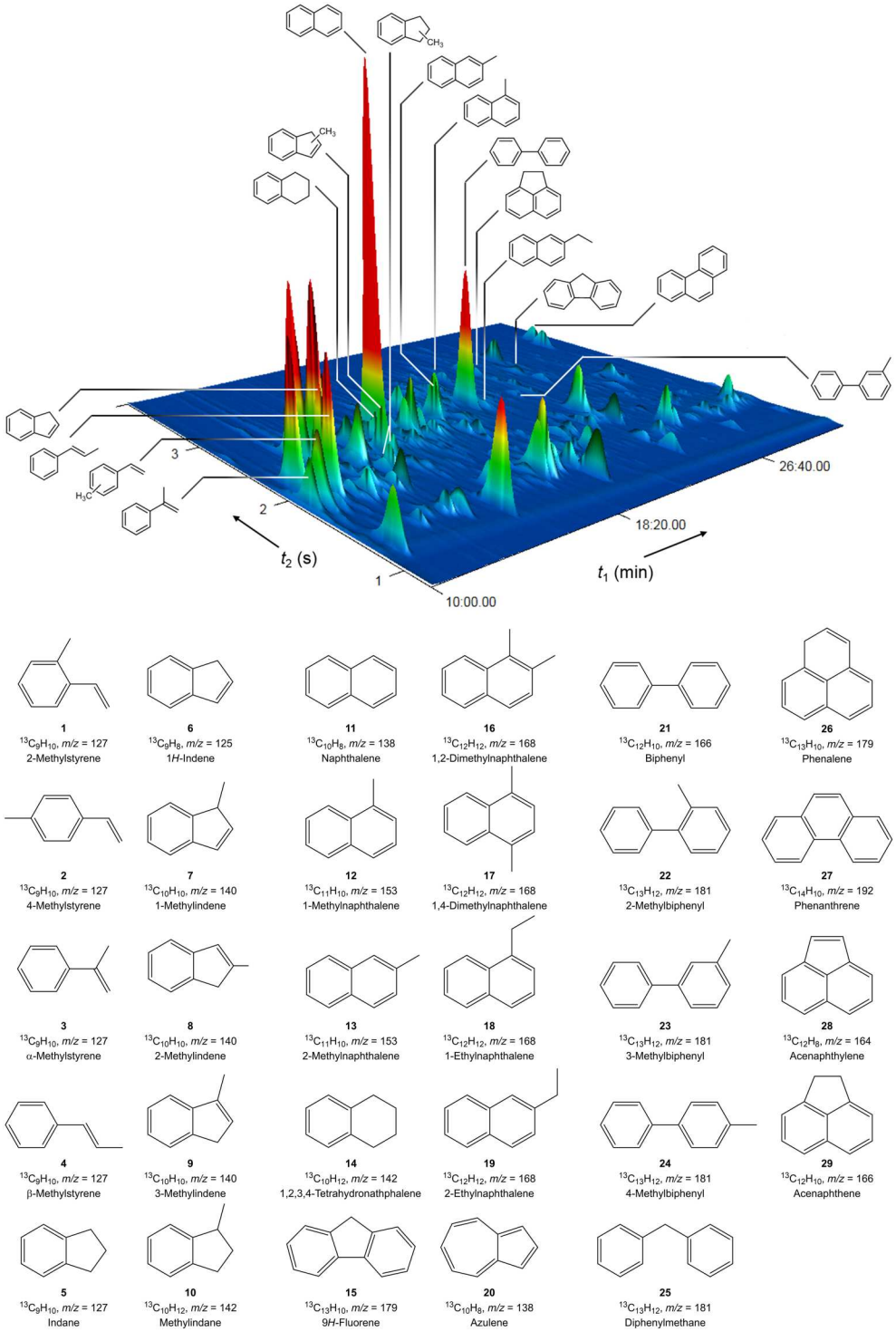

Fig. 6. Aromatic compounds were detected from the residues of the ^{13}C-acetylene ($^{13}C_2H_2$) ices irradiated at 8.2 eV amu^{-1} by multidimensional gas chromatography along with their detailed structure, name, and molecular masses. Quantification of the detected species is provided in table S8.

0.1% and 46.7 ± 1.5% of the expected hydrogen production for methane and acetylene, respectively (table S7), suggesting that the ices still store molecular hydrogen. Consequently, mass spectroscopic evidence suggests an enhanced carbon-to-hydrogen ratio of the KBO analog surfaces with rising exposure time to GCR proxies, which is required for extended conjugated π-bond systems. This process is accompanied not only by reddening (Fig. 1) but also by optical color changes from gray to yellow and brownish to black (Fig. 2C)

$$2\ CH_4 \rightarrow C_2H_2 + 3\ H_2 \quad (3)$$

$$3\ C_2H_2 \rightarrow C_6H_6 \quad (4)$$

$$C_6H_6 + 2\ C_2H_2 \rightarrow C_{10}H_8 + H_2 \quad (5)$$

In conclusion, the analysis of the infrared spectra along with the kinetics profiles reveals aromatic moieties as likely chromophores and potential molecular building blocks of the polymeric residue that explain the darkening and reddening of the exposed model ices (Figs. 1 and 2), formed over geological time scales of at least 130 million years for acetylene and 1100 million years for methane (Fig. 4). However, because FTIR can only extract information of functional groups, the analyses were extended to identify individual aromatic molecules formed in the radiation exposure of the KBO analog surfaces by two-dimensional GC×GC-TOF-MS and TOF-SIMS.

Two-dimensional GC×GC-TOF-MS

Exposure of the KBO model ices to doses up to 82.1 eV amu^{-1} methane and acetylene, respectively, followed by annealing of the irradiated samples to 300 K results in the formation of solid residues. The soluble fractions of irradiated acetylene residues were analyzed via GC×GC-TOF-MS, and aromatic compounds were identified through cross-correlation of the dual retention times ($R_{t1} \times R_{t2}$) and mass-to-charge ratios of the ionized organics with known standards (Materials and Methods). A typical dataset is presented in Fig. 6 where nearly 30 discrete molecules are identified (table S8). These include mono- to tricyclic aromatics comprising substituted benzenes, naphthalenes, and biphenylenes, as well as phenanthrene, phenalene, acenaphthylene, and 9*H*-fluorene. Methyl (—CH_3), ethyl (—C_2H_5), vinyl (—C_2H_3), and allyl (—C_3H_5) side groups were identified. These C1 to C3 side chains act as potential linkers to connect individual aromatic molecules to more complex, potentially macromolecular (*tholins*)–like and hence nonsoluble organic structures. Quantitatively spoken, the derivatives of the bicyclic moieties of 1*H*-indene (C_9H_8), naphthalene ($C_{10}H_8$), and biphenyl ($C_{12}H_{10}$) represent the dominant aromatics synthesized with quantities in the 20 to 50 pmol range, i.e., conversion efficiencies of up to 10^{-3}% to individual, soluble aromatics with respect to acetylene. The tricyclic aromatics have yields between one [9*H*-fluorene ($C_{13}H_{10}$), phenanthrene ($C_{14}H_{10}$)] and two [acenaphthylene ($C_{12}H_8$)] orders of magnitude lower that the bicyclic species. Dimethyl-substituted naphthalenes ($C_{12}H_{12}$) depict notably diminished yields compared to their mono-substituted (methyl, ethyl) counterparts. These findings suggest stepwise molecular mass growth processes, not only from mono- to bi- and tricyclic aromatic systems via ring annulation but also from pure aromatic molecules to mono- and dialkylated derivatives of PAHs (*81*, *82*). However, with the exception of the blue azulene ($C_{10}H_8$), the entire inventory of aromatics identified is colorless and hence cannot account for the enhancement due to their insufficiently delocalized π electron system. Therefore, to account for the experimental observations of increased color slopes and reddening over geological time scales, the radiolysis of the KBO analog ices likely converts these simple mono-, bi-, and tricyclic aromatics to more complex and insoluble aromatic systems as also inferred from the aforementioned FTIR data, i.e., the conversion of aromatic C—H functional groups at doses exceeding 10 eV amu^{-1}.

Time-of-flight secondary ion mass spectrometry

The insoluble fraction of the organic residues, inaccessible for gas chromatographic approaches such as GC×GC-TOF-MS, was analyzed via TOF-SIMS (*83*, *84*). TOF-SIMS sputters the surface of the organic residues with a focused ion beam (Bi_3^+) and collects the ejected secondary cations and anions. Therefore, even molecular building blocks such as aromatics linked through chains can be sputtered, and their cationic and anionic fragments can be released into the gas phase (figs. S5 and S6 and tables S9 and S10). First, the TOF-SIMS analysis reveals the presence of unsubstituted and substituted monocyclic (C_5H_5, C_6H_6, C_7H_7, C_8H_7), bicyclic (C_9H_7, $C_{10}H_8$, $C_{12}H_8$), and tricyclic aromatic moieties ($C_{13}H_9$, $C_{15}H_9$) in the insoluble residues. Second, various acyclic and unsaturated C2 to C4 substituents (C_2H_3, C_3H_3, C_4H_3, C_4H_5) could be identified in the cation fragments. Last, two classes of highly unsaturated, hydrogen-terminated anionic carbon chains could be sampled: polyacetylene structures and cumulenes with formally one proton removed. Together, TOF-SIMS data reveal the presence of fundamental aromatic building blocks carrying up to three rings and of highly unsaturated linear "linker" moieties connecting these aromatic motives. The unsaturated nature of these linkers is vital in expanding the system of delocalized π electrons, leading to the reddening of the analog ices as the exposure to the GCR proxies advances.

DISCUSSION

This study provides a first step toward a systematic understanding of the mechanisms of the reddening of icy hydrocarbon surfaces in the outer solar system through the conversion of simple organics like methane and acetylene to PAHs embedded in reddish and even black polymer matrices. First, the laboratory simulation experiments provide compelling evidence concerning the radiation-induced reddening and optical darkening from white via yellow and brownish to black of KBO analog ices of methane and acetylene ices over geological time scales of up to 1800 million years. These findings are consistent with the colors of KBOs with $B - V = 0.7$ to 1.3 and $V - R = 0.3$ to 0.8, respectively. Typical KBOs within these color ranges are compiled in table S11, are located at distances from 39 to 44 AU from the Sun, and comprise, e.g., Makemake, Orcus, and Salacia. The highest dose (longest exposure age) colors produced by irradiation are redder than observed in nature, particularly for the products of irradiated acetylene. This could mean that the effective exposure ages of the KBOs are limited, perhaps by gardening due to micrometeorite bombardment, as is observed on the Moon. Alternatively, it could indicate that acetylene occupies only

a small fraction of the KBO surface such that its strongly reddened radiation-produced products are diluted by hemispheric mixing with less red material. For example, irradiated acetylene ice could be diluted with coprecipitating methane and other volatile hydrocarbons, suppressing the extreme reddening of the former.

Second, while the colors of hydrocarbon residues depend strongly on dose, thus underlining the critical role of GCR exposure of KBO hydrocarbon ices, they are invariant with respect to temperature as the samples are heated from 10 to 300 K. This contrasts with the empirical absence of ultrared colors in comets and other bodies arriving from the outer solar system (*6*, *12*–*14*). We conclude that irradiated material formed in the Kuiper Belt is either removed during transport to the inner solar system by ejection or buried under fallback debris, as surmised earlier based on telescopic data (*13*).

Third, on the molecular level, aromatic moieties carrying up to three rings as in phenanthrene ($C_{14}H_{10}$), phenalene (C_9H_{10}), and acenaphthylene ($C_{12}H_8$), whose π electrons are extensively delocalized via unsaturated linkers, play a vital factor in the reddening of KBO surfaces, thus defining the level of molecular complexity synthesized in the evolution of our solar system since the time of formation. The reddening and darkening along with the increase of the carbon-to-hydrogen ratio of the exposed organic matter is also supported by the release of molecular hydrogen into the gas phase. This essentially depletes the ices in hydrogen, leaving behind carbon-enriched organics. Although our studies focused on airless bodies, these results have also an important start for understanding Pluto's black to reddish regions such as Cthulhu Macula as well as its yellowish topologies detected in Lowell Regio and Sputnik Planitia (*68*).

Last, due to the chemical and physical conditions of airless bodies in the outer solar system environments, there is no single experiment that can mimic the complexity of the surface composition and irradiation environments. Exploiting the experimental and analytical protocol developed here, further experiments should expand on the ice composition such as the systematic incorporation of nitrogen, methanol, and water from binary via ternary and even more complex systems, and also on probing the effects of mineral additives on the reddening and on the microscopic reaction mechanisms. This is critical because, besides hydrocarbons (CH_4, C_2H_2) as investigated in the present work, water (H_2O), ammonia (NH_3), nitrogen (N_2), carbon monoxide (CO), carbon dioxide (CO_2), and methanol (CH_3OH) have been detected on surfaces of KBOs (*50*). Exposure of these mixtures to ionizing radiation might access color-color regions beyond the $B - V = 0.7$ to 1.3 and $V - R = 0.3$ to 0.8 regime (Fig. 2B), which cannot be replicated by the GCR processing of hydrocarbon ices. Ideally, the incorporation of oxygen- and nitrogen-bearing molecules in ices should systematically map out the color diversity of KBOs by correlating distinct ice compositions with the astronomically observed color variances. In addition, combined GCR proxy-photon irradiations are desirable to explore individual, but also cumulative effects on the chemical processing of KBO surfaces and how this influences their colors. These synergistic effects are expected to develop the concepts of how complex molecules could have been synthesized in the outer solar system, ultimately leading to a better understanding of the origin and evolution of our solar system.

MATERIALS AND METHODS

The irradiation experiments were performed in an ultrahigh-vacuum chamber evacuated to a base pressure of 1×10^{-11} torr by magnetically suspended turbo molecular pumps backed by an oil-free scroll pump (*60*). In the chamber, a polished silver wafer was attached to an oxygen-free high-conductivity copper cryostat via indium foil and connected to a two-stage closed-cycle helium refrigerator (CTI-Cryogenics Cryodyne 1020, compressor: CTI-Cryogenics 9600). By using a doubly differentially pumped rotational feedthrough, the substrate can be rotated in the horizontal plane. The temperature of the silver wafer was monitored by a silicon diode sensor (Lakeshore DT-470) and regulated in a range of 10 to 300 K with a precision of ±0.3 K by a programmable temperature controller (Lakeshore 336). When the substrate has been cooled to 10 K, ^{13}C-acetylene ($^{13}C_2H_2$, AirGas, >99.9%) or ^{13}C-methane ($^{13}CH_4$, AirGas, >99.9%) was deposited onto the substrate via a glass capillary array. The main goal of our research is the identification of (aromatic) hydrocarbons. Note that aromatic molecules are widespread in the environment. Therefore, to eliminate any potential contaminants, ^{13}C-labeled reactants were used. This results in fully ^{13}C-labeled aromatics, which are not present in the environment. Therefore, any fully ^{13}C-labeled molecule must be the result of the radiation processing of the ices. On the basis of the refractive index (n) of 1.34 for solid acetylene and 1.30 for solid methane (*74*, *85*), the thicknesses of the ices were calculated to be 750 ± 60 nm (*86*). After deposition, the $^{13}C_2H_2$ or $^{13}CH_4$ ice was isothermally processed by 5-keV electrons (Specs EQ 22-35 electron source) simulating secondary electrons formed in the track of GCRs penetrating the ices for different durations (table S1). The electron incidence angle is 70° to the ice surface normal. Using Monte Carlo simulations (CASINO 2.42), the average depths of the electrons were estimated to be 320 ± 30 nm for $^{13}C_2H_2$ and 330 ± 30 nm for $^{13}CH_4$, which are less than the ice thickness (750 ± 60 nm), thus avoiding interaction between the electrons and the silver wafer. Here, the electrons were calculated to deposit average doses of 82.1 ± 10 eV amu^{-1} into the $^{13}C_2H_2$ and $^{13}CH_4$ ices (table S1). Upon completion of irradiation, temperature-programmed desorption studies were carried out by heating the substrate to 300 K at a rate of 1 K min^{-1}. The $^{13}C_2H_2$ and $^{13}CH_4$ ices were analyzed in situ before, during, and after processing with an FTIR spectrometer (Nicolet 6700) and a UV-vis spectrometer (Nicolet Evolution 300). The FTIR spectrometer was operated in absorption-reflection-absorption mode at a reflection angle of 45°, and the infrared region of 5000 to 500 cm^{-1} was monitored, using a resolution of 4 cm^{-1}. Simultaneously, the focused light of the UV-vis spectrometer was reflected off of the silver wafer at an angle of 30° and focused onto a photodiode that was shielded from ambient light. The absorption spectra in the range of 190 to 1100 nm were recorded with a resolution of 4 nm. FTIR analyses allowed for the vibrational modes of the reactants and products to be monitored during the experiment, while UV-vis probed the electronic transitions present. In addition, during all of the experiments, mass spectra of the gas-phase species were recorded using an Extrel 5221 QMS operating in residual-gas-analyzer mode with an electron impact ionization energy of 70 eV. The absorption bands of UV-vis spectra are superimposed by strong interference features. Because the thickness and refractive index of the films slightly changed during the irradiation, a simple subtraction of the two spectra cannot be applied to remove the interference

bands. To obtain experimental UV-vis spectra free from interference patterns, the interference was derived theoretically by using a "two interfaces between three media" model generalized for complex refractive indices $n_i + ik_i$ (*87*). To analyze and assign the peaks generated during the irradiation of acetylene and methane ices, we deconvoluted its FTIR spectra via the *Fityk* program (Fig. 4, figs. S2 to S4, and tables S2 to S5). Furthermore, to determine the temporal evolution of the functional group formed within the ices during the irradiation, quantitatively, we integrated key absorption features: ν_3 mode (2999 cm^{-1}) of methane with an integral absorption coefficient of 1.41×10^{-17} cm $molecule^{-1}$ (*88*), ν_3 mode of acetylene (3222 cm^{-1}) with an integral absorption coefficient of 2.39×10^{-17} cm $molecule^{-1}$ (*74*), and the C—H stretching mode (3068 and 3070 cm^{-1}) of aromatic species with an integral absorption coefficient of 2.10×10^{-18} cm $molecule^{-1}$ (*77*), and then calculated the column density, i.e., the numbers of absorbing molecules per cm^2, N, through a modified Lambert-Beer relationship (*86*). In detail, for the $^{13}C_2H_2$ ice, a reversible reaction to first-order aromatics (aromatics$_1$) was considered, with rates described by rate constants k_1 and k_{-1} through a multistep reaction as below

$$^{13}C_2H_2 \underset{k_{-1}}{\overset{k_1}{\rightleftharpoons}} \text{Aromatics}_1 \xrightarrow{k_2} \text{Aromatics}_2 \longrightarrow \text{Polymeric aromatics}$$

The concentration of those aromatics was found to quickly increase and then sharply decrease (k_2) to form the second-order aromatics (aromatics$_2$) with overlapping infrared band intensity. For the $^{13}CH_4$ ice, a more complex reaction scheme was necessary to fit temporal profiles. Here, $^{13}CH_4$ reacts to $^{13}C_2H_2$ (k_1) with the formed $^{13}C_2H_2$ producing aromatics$_1$ (k_2). However, a separate reaction from $^{13}CH_4$ to aromatics$_1$ (k_3) had to be introduced, too, where within the error limits both k_1 and k_2 were essentially in the same range (table S6). Subsequently, these aromatics$_1$ further reacted to second-generation (more complex) aromatics$_2$ (k_4). In this case, the temporal profile for $^{13}C_2H_2$ displays further contribution to the ν(CH) band intensity after $^{13}C_2H_2$ would be depleted; hence, an additional reaction pathway from $^{13}CH_4$ to polyacetylenes (k_5) was included to account for the discrepancy. While the column density of $^{13}CH_4$ and $^{13}C_2H_2$ can be determined from integrated absorption coefficients, various compounds with different numbers of absorption carriers and coefficients contribute to the temporal profile for aromatic ν(CH). Therefore, absolute column densities for the aromatics were not calculated, but the outputs from kinetically fitting their precursors ($^{13}CH_4$ and $^{13}C_2H_2$) were scaled to fit the integrated peak areas. The optimized rate constants (k) obtained by kinetically fitting the data using first-order reactions are shown in table S6.

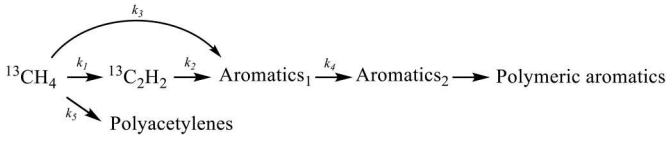

This section details the quantification of molecular hydrogen outgassing during the irradiation of the hydrocarbon ices. An Extrel 5221 QMS operating in the residual-gas-analyzer mode with an electron impact ionization energy of 70 eV at a 2-mA emission current was exploited; the secondary electron multiplier was operated at 1800 and 1900 V for acetylene and methane ices, respectively. Because the QMS signal is an amplified current generated from the ions, it is necessary to determine the proportionality constant (K) between the number of hydrogen molecules (n) in the gas phase and QMS signal recorded in ampere (A) (*89*). Following the procedure as detailed in (*89*), these constants were derived to $K_{H2} = (8.41 \pm 0.4) \times 10^6$ molecule $counts^{-1}$ for 1800 V and $(5.76 \pm 0.3) \times 10^6$ molecule $counts^{-1}$ for 1900 V, respectively. The number of hydrogen molecules is then extracted through

$$n_{H2} = K_{H2} \int_0^t A_{H2} dt$$

where $\int_0^t A_{H2} dt$ is the integrated counts of QMS signal [mass charge ratio (m/z) = 2] recorded during the irradiation of acetylene and methane ices and listed in table S7.

Two-dimensional gas chromatography time-of-flight mass spectrometry

Analytical standards

High-purity analytical standards were acquired from Sigma-Aldrich (Merck, Schnellendorf, Germany) and dissolved in dichloromethane (DCM). Final concentrations of standard mixtures were prepared at five levels in the range of 10^{-5} to 10^{-9} g $liter^{-1}$ per compound to ensure reference spectra, retention time data, and calibration curves without ion source or column overload as well as standard concentrations representing those found in the interstellar ice analog samples. Target PAHs for identification and calibration were obtained in a 16-component mix QTM PAH Mix including 16 US Environmental Protection Agency (EPA) PAHs (acenaphthene, acenaphthylene, anthracene, benz[*a*]anthracene, benzo[*b*]fluoranthene, benzo[*ghi*]perylene, benzo[*a*]pyrene, 2-bromonaphthalene, chrysene, dibenz[*a,h*]anthracene, fluoranthene, fluorene, indeno[1,2,3-*cd*]pyrene, naphthalene, phenanthrene, and pyrene). Additional reference standards included phenylacetylene, 2-methylstyrene, 4-methylstyrene, indane, indene, 1,3-diethynylbenzene, 2-methylindene, 1,2,3,4-tetrahydronaphthalene, 1,2-dihydronaphthalene, 2-methylnaphthalene, azulene, 1-methylnaphthalene, cyclohexylbenzene, biphenyl, 2-methylbiphenyl, 4-methylbiphenyl, 1-ethylnaphthalene, 2-ethylnaphthalene, diphenylmethane, 2-vinylnaphthalene, 1,2-dimethylnaphthalene, 1,4-dimethylnaphthalene, biphenylene, cis-stilbene, trans-stilbene, 3,3′-dimethylbiphenyl, 4,4′dimethylbiphenyl, 4-vinylbiphenyl, 2-ethynylnaphthalene, 2-phenylindene, and coronene. An internal standard, methyl laurate (10^{-5} M), was added to the reference standards and all ice analog samples to verify injection and elution consistency. All solvents were of chromatographic (high-performance liquid chromatography) or American Chemical Society (ACS) grade. Glassware was rinsed thoroughly before with ethanol and Milli-Q water and heated in a furnace at 500°C for 5 hours.

Sample extraction

Irradiated samples were extracted from their support using different organic solvents to extract the maximum of the refractory organic residues. Large fractions of the residues, however, were insoluble in the organic solvents used and, after various extraction procedures, were applied to improve sample recoveries and solvation including agitation, ultrasonic bath, and hydrolysis at elevated temperatures. Briefly, the residue sample with a dose of 8.2 eV amu^{-1} was extracted with DCM, hexane, acetone/hexane 1:1 (v/v), and chloroform.

The sample was then vortexed and dried under a gentle stream of nitrogen, and 50 μl of the internal standard solution in DCM was added directly to the reaction vial before being heated at 80°C for 24 hours. One sample blank was prepared following the same procedure extracting a nonirradiated polished silver mirror that has been mounted into the stainless-steel chamber. The use of different organic solvents to maximize the recovery of refractory residue constituents was inefficient but increased the risk of contamination. The residue samples from the lower-dose irradiated ices were therefore extracted using DCM only. All samples were centrifuged after heating or ultrasonic treatment, and the supernatant of all sample mixtures was quantitatively transferred into 2-ml GC vials equipped with 250-μl glass inserts for subsequent multidimensional gas chromatographic analyses. Each individual ice analog sample was accompanied by its reagent blank by using identical quantities of organic solvents and procedures (heating and ultrasonic bath) used for sample extraction.

GC×GC-TOF-MS analyses

Analyses were performed on a LECO Pegasus BT two-dimensional gas chromatograph, fitted with a dual cryogenic jet modulator, coupled to a time-of-flight mass spectrometer (GC×GC-TOF-MS). The GC×GC was equipped with an Rxi-5MS (30 m × 0.25 mm internal diameter, 0.25 μm film thickness d_f, Restek) first dimension (^{1}D) column, coupled to an Rxi-17SilMs (1.6 m × 0.25 mm inside diameter, 0.25 μm d_f, Restek) ^{2}D column. Carrier gas flow of helium through the columns was 1 ml min^{-1}. A liquid autosampler (Agilent model 7693A) was used to inject 1 μl of extract or standard volumes in splitless mode for 90 s at 300°C. The GC oven was held at 40°C for 1 min and increased at 5°C min^{-1} to a maximum of 320°C and held for 5 min. The ion source was operated at 230°C and the transfer line temperature at 340°C, with spectra summed to give a data rate of 100 spectra s^{-1} in electron ionization mode at 70 eV. The scan range was from 50 to 500 μ. The modulation and data recording were commenced at 8.00 min (solvent delay). The modulation period was 5 s, and the cryogenic jet modulator was held in the release mode for 1.5 s. Data were processed using LECO ChromaTOF v.5.31.16 software, optimized for the Pegasus system, analyzing the target ions for identification and quantification using the unique mass. The modulated peak areas were obtained from both manual integration and automatic software integration. For all reference standards, a linear fit was used, with correlations yielding $r^2 \geq 0.99$.

All analytical runs and sample runs (including procedural blanks) were bracketed by solvent (DCM) blanks. Solvent blanks were at or near noise level and did show no evidence of carryover. Identification of PAHs and related compounds in interstellar analog ices was performed on direct comparison of retention times (t_R), retention indices (RI), as well as mass spectral data with standards. With the availability of the National Institute of Standards and Technology (NIST) mass spectral library and reported retention indices, we (tentatively) identified several more compounds without the injection of reference standards with overall high confidence based on retention time alignment, signal/noise ratios, m/z accuracy, and spectral quality.

Retention indices (RI) for reference compounds and single target compounds in the analog ice samples were calculated using the programmed-temperature retention index (*90*) in Lee index scale (*91*, *92*) based on naphthalene (RI = 200) and phenanthrene (RI = 300) eluting in the retention time window of expected target molecules

$$\mathrm{RI} = 100 \times \frac{t_{R(\mathrm{target})} - t_{R(z)}}{t_{R(z+1)} - t_{R(z)}} + 100 \times z$$

where $R_{t(\mathrm{target})}$ is the retention time of the substance for which the retention index is to be determined and z and $z + 1$ are the numbers of aromatic rings in the interpolation interval eluting before and after the substance of interest with their corresponding retention times, $R_{t(z)}$ and $R_{t(z+1)}$, respectively.

Time-of-flight secondary ion mass spectrometry

The insoluble residues were analyzed using a TOF-SIMS instrument (TOF-SIMS 5-300, ION-TOF) equipped with a reflectron mass analyzer, a 30-keV Bi_n liquid metal primary ion source (Bi-LMIG), and a low-energy electron flood gun. Spectra were acquired with Bi_3^+ in bunched mode with a focus of 2 to 3 mm, a beam current of 0.25 pA, and a total dose of 1.25×10^8 ions. Data were acquired from a 500-μm^2 analysis area. The positive and negative ions from the sputtered residue were recorded, and the mass spectra from TOF-SIMS were analyzed. A Python code was used to filter noise and potentially weak and hence ambiguous peaks. The code adds counts in the vicinity dx of $^{13}C_xH_y$ masses for the mass to charge in the range of 0 to 500 amu, where dx is M/5000 determined by the resolution of the mass spectrometer. The vertical cutoff is 200 counts, i.e., mass channels with less than 200 counts are background based on blank experiments. The Python code can be found in the Supplementary Materials.

Supplementary Materials

This PDF file includes:

Python code for SIMS
Figs. S1 to S6
Tables S1 to S11

REFERENCES AND NOTES

1. D. Jewitt, J. Luu, Discovery of the candidate Kuiper Belt object 1992 QB1. *Nature* **362**, 730–732 (1993).
2. H. A. Weaver, W. C. Gibson, M. B. Tapley, L. A. Young, S. A. Stern, in *New Horizons: Reconnaissance of the Pluto-Charon System and the Kuiper Belt*, C. T. Russell, Eds. (Springer New York, 2009), pp. 75–91.
3. S. A. Stern, H. A. Weaver, J. R. Spencer, H. A. Elliott, The *New Horizons* Kuiper Belt extended mission. *Space Sci. Rev.* **214**, 77 (2018).
4. N. Pinilla-Alonso, J. A. Stansberry, B. J. Holler, in *The Trans-Neptunian Solar System*, D. Prialnik, A. Barucci, L. Young, Eds. (Elsevier, 2020), chap. 18, pp. 395–412.
5. A. Morbidelli, D. Nesvorný, in *The Trans-Neptunian Solar System*, D. Prialnik, A. Barucci, L. Young, Eds. (Elsevier, 2020), chap. 2, pp. 25–59.
6. D. C. Jewitt, J. X. Luu, Colors and spectra of Kuiper Belt objects. *Astrophys. J.* **122**, 2099–2114 (2001).
7. M. Fulchignoni, I. Belskaya, M. A. Barucci, M. C. De Sanctis, A. Doressoundiram, in *The Solar System Beyond Neptune*, M. A. Barucci, H. Boehnhardt, D. P. Cruikshank, A. Morbidelli, Eds. (University of Arizona Press, 2008), pp. 181–192.
8. M. A. Barucci, F. Merlin, in *The Trans-Neptunian Solar System*, D. Prialnik, A. Barucci, L. Young, Eds. (Elsevier, 2020), chap. 5, pp. 109–126.
9. N. Peixinho, P. Lacerda, D. Jewitt, Color-inclination relation of the classical Kuiper Belt objects. *Astron. J.* **136**, 1837–1845 (2008).
10. A. Alvarez-Candal, C. Ayala-Loera, R. Gil-Hutton, J. L. Ortiz, P. Santos-Sanz, R. Duffard, Absolute colours and phase coefficients of trans-Neptunian objects: Correlations and populations. *Mon. Not. R. Astron. Soc.* **488**, 3035–3044 (2019).
11. N. Peixinho, A. Delsanti, A. Guilbert-Lepoutre, R. Gafeira, P. Lacerda, The bimodal colors of Centaurs and small Kuiper Belt objects. *Astron. Astrophys.* **546**, A86 (2012).
12. J. Luu, D. Jewitt, Color diversity among the Centaurs and Kuiper Belt objects. *Astron. J.* **112**, 2310 (1996).

13. D. C. Jewitt, From Kuiper Belt object to cometary nucleus: The missing ultrared matter. *Astron. J.* **123**, 1039–1049 (2002).
14. D. Jewitt, Color systematics of comets and related bodies. *Astron. J.* **150**, 6 (2015).
15. D. Jewitt, in *Trans-Neptunian Objects and Comets* (Springer, ed. 1, 2008), pp. 1–78.
16. M. Duncan, H. Levison, L. Dones, in *COMETS II*, M. Festou, H. U. Keller, H. A. Weaver, Eds. (University of Arizona Press, 2004), pp. 193–204.
17. P. D. Holtom, C. J. Bennett, Y. Osamura, N. J. Mason, R. I. Kaiser, A combined experimental and theoretical study on the formation of the amino acid glycine (NH_2CH_2COOH) and its isomer ($CH_3NHCOOH$) in extraterrestrial ices. *Astrophys. J.* **626**, 940–952 (2005).
18. F. Goesmann, H. Rosenbauer, J. H. Bredehöft, M. Cabane, P. Ehrenfreund, T. Gautier, C. Giri, H. Krüger, L. Le Roy, A. J. MacDermott, S. McKenna-Lawlor, U. J. Meierhenrich, G. M. M. Caro, F. Raulin, R. Roll, A. Steele, H. Steininger, R. Sternberg, C. Szopa, W. Thiemann, S. Ulamec, Organic compounds on comet 67P/Churyumov-Gerasimenko revealed by COSAC mass spectrometry. *Science* **349**, aab0689 (2015).
19. K. Altwegg, H. Balsiger, A. Bar-Nun, J.-J. Berthelier, A. Bieler, P. Bochsler, C. Briois, U. Calmonte, R. Combi Michael, H. Cottin, J. De Keyser, F. Dhooghe, B. Fiethe, A. Fuselier Stephen, S. Gasc, I. Gombosi Tamas, C. Hansen Kenneth, M. Haessig, A. Jäckel, E. Kopp, A. Korth, L. Le Roy, U. Mall, B. Marty, O. Mousis, T. Owen, H. Rème, M. Rubin, T. Sémon, C.-Y. Tzou, J. Hunter Waite, P. Wurz, Prebiotic chemicals—amino acid and phosphorus—in the coma of comet 67P/Churyumov-Gerasimenko. *Sci. Adv.* **2**, e1600285 (2016).
20. K. Altwegg, H. Balsiger, J. J. Berthelier, A. Bieler, U. Calmonte, S. A. Fuselier, F. Goesmann, S. Gasc, T. I. Gombosi, L. Le Roy, J. de Keyser, A. Morse, M. Rubin, M. Schuhmann, M. G. G. T. Taylor, C. Y. Tzou, I. Wright, Organics in comet 67P—A first comparative analysis of mass spectra from ROSINA-DFMS, COSAC and Ptolemy. *Mon. Not. R. Astron. Soc.* **469**, S130–S141 (2017).
21. M. A.-O. Rubin, C. A.-O. Engrand, C. A.-O. Snodgrass, P. Weissman, K. A.-O. Altwegg, H. A.-O. Busemann, A. A.-O. Morbidelli, M. A.-O. X. Mumma, On the origin and evolution of the material in 67P/Churyumov-Gerasimenko. *Space Sci. Rev.* **206**, 102 (2020).
22. M. Läuter, T. Kramer, M. Rubin, K. Altwegg, The gas production of 14 species from comet 67P/Churyumov-Gerasimenko based on DFMS/COPS data from 2014 to 2016. *Mon. Not. R. Astron. Soc.* **498**, 3995–4004 (2020).
23. W. M. Grundy, Is the missing ultra-red material colorless ice? *Icarus* **199**, 560–563 (2009).
24. M. E. Brown, E. L. Schaller, W. C. Fraser, A hypothesis for the color diversity of the Kuiper Belt. *Astrophys. J.* **739**, L60 (2011).
25. C. M. Dalle Ore, M. A. Barucci, J. P. Emery, D. P. Cruikshank, C. de Bergh, T. L. Roush, D. Perna, F. Merlin, L. V. Dalle Ore, The composition of "ultra-red" TNOs and centaurs. *Icarus* **252**, 311–326 (2015).
26. I. Wong, M. E. Brown, The bimodal color distribution of small Kuiper Belt objects. *Astron. J.* **153**, 145 (2017).
27. M. A. Barucci, F. Merlin, E. Dotto, A. Doressoundiram, C. de Bergh, TNO surface ices. Observations of the TNO 55638 (2002 VE_{95}) and analysis of the population's spectral properties. *Astron. Astrophys.* **455**, 725–730 (2006).
28. S. D. Benecchi, D. Borncamp, A. H. Parker, M. W. Buie, K. S. Noll, R. P. Binzel, S. A. Stern, A. J. Verbiscer, J. J. Kavelaars, A. M. Zangari, J. R. Spencer, H. A. Weaver, The color and binarity of (486958) 2014 MU69 and other long-range New Horizons Kuiper Belt targets. *Icarus* **334**, 22–29 (2019).
29. C. Sagan, B. N. Khare, Tholins: Organic chemistry of interstellar grains and gas. *Nature* **277**, 102–107 (1979).
30. D. P. Cruikshank, H. Imanaka, C. M. Dalle Ore, Tholins as coloring agents on outer Solar System bodies. *Adv. Space Res.* **36**, 178–183 (2005).
31. H. Imanaka, B. N. Khare, J. E. Elsila, E. L. O. Bakes, C. P. McKay, D. P. Cruikshank, S. Sugita, T. Matsui, R. N. Zare, Laboratory experiments of Titan tholin formed in cold plasma at various pressures: Implications for nitrogen-containing polycyclic aromatic compounds in Titan haze. *Icarus* **168**, 344–366 (2004).
32. C. M. Dalle Ore, M. Fulchignoni, D. P. Cruikshank, M. A. Barucci, R. Brunetto, H. Campins, C. de Bergh, J. H. Debes, E. Dotto, J. P. Emery, W. M. Grundy, A. P. Jones, V. Mennella, F. R. Orthous-Daunay, T. Owen, I. Pascucci, Y. J. Pendleton, N. Pinilla-Alonso, E. Quirico, G. Strazzulla, Organic materials in planetary and protoplanetary systems: Nature or nurture? *Astron. Astrophys.* **533**, A98 (2011).
33. W. M. Grundy, J. A. Stansberry, Mixing models, colors and thermal emissions. *Earth Moon Planets* **92**, 331–336 (2003).
34. W. Grundy, K. Noll, D. Stephens, Diverse albedos of small trans-Neptunian objects. *Icarus* **176**, 184–191 (2005).
35. A. J. Verbiscer, S. Porter, S. D. Benecchi, J. J. Kavelaars, H. A. Weaver, J. R. Spencer, M. W. Buie, D. Tholen, B. J. Buratti, P. Helfenstein, A. H. Parker, C. B. Olkin, J. Parker, S. A. Stern, L. A. Young, K. Ennico-Smith, K. N. Singer, A. F. Cheng, C. M. Lisse, Phase curves from the Kuiper belt: Photometric properties of distant kuiper belt objects observed by *New Horizons*. *Astron. J.* **158**, 123 (2019).
36. J. D. Hofgartner, B. J. Buratti, P. O. Hayne, L. A. Young, Ongoing resurfacing of KBO Eris by volatile transport in local, collisional, sublimation atmosphere regime. *Icarus* **334**, 52–61 (2019).
37. A. M. Turner, R. I. Kaiser, Exploiting photoionization reflectron time-of-light mass spectrometry to explore molecular mass growth processes to complex organic molecules in interstellar and solar system ice analogs. *Acc. Chem. Res.* **53**, 2791–2805 (2020).
38. C. de Bergh, B. Schmitt, L. V. Moroz, E. Quirico, D. P. Cruikshank, in *The Solar System Beyond Neptune*, M. A. Barucci, H. Boehnhardt, D. P. Cruikshank, A. Morbidelli, Eds. (University of Arizona Press, 2008), pp. 483–506.
39. R. Hudson, M. E. Palumbo, G. Strazzulla, M. Moore, J. Cooper, S. Sturner, in *The Solar System Beyond Neptune,* M. A. Barucci, H. Boehnhardt, D. P. Cruikshank, A. Morbidelli, Eds. (University of Arizona Press, 2008), pp. 507–523.
40. M. J. Poston, A. Mahjoub, B. L. Ehlmann, J. Blacksberg, M. E. Brown, R. W. Carlson, J. M. Eiler, K. P. Hand, R. Hodyss, I. Wong, Visible near-infrared spectral evolution of irradiated mixed ices and application to Kuiper Belt objects and Jupiter Trojans. *Astrophys. J.* **856**, 124 (2018).
41. S. C. Tegler, W. Romanishin, S. J. G. J. Consolmagno, Two color populations of Kuiper Belt and Centaur objects and the smaller orbital inclinations of red Centaur objects. *Astron. J.* **152**, 210 (2016).
42. S. C. Tegler, W. Romanishin, Extremely red Kuiper-belt objects in near-circular orbits beyond 40 AU. *Nature* **407**, 979–981 (2000).
43. S. C. Tegler, W. Romanishin, Two distinct populations of Kuiper Belt objects. *Nature* **392**, 49–51 (1998).
44. G. Andronico, G. A. Baratta, F. Spinella, G. Strazzulla, Optical evolution of laboratory-produced organics—Applications to Phoebe, Iapetus, outer belt asteroids and cometary nuclei. *Astron. Astrophys.* **184**, 333–336 (1987).
45. R. Brunetto, M. A. Barucci, E. Dotto, G. Strazzulla, Ion irradiation of frozen methanol, methane, and benzene: Linking to the colors of Centaurs and trans-Neptunian objects. *Astrophys. J.* **644**, 646–650 (2006).
46. W. R. Thompson, B. G. J. P. T. Murray, B. N. Khare, C. Sagan, Coloration and darkening of methane clathrate and other ices by charged particle irradiation: Applications to the outer solar system. *J. Geophys. Res.* **92**, 14933–14947 (1987).
47. C. J. Bennett, C. Pirim, T. M. Orlando, Space-weathering of solar system bodies: A laboratory perspective. *Chem. Rev.* **113**, 9086–9150 (2013).
48. R. G. Urso, D. Baklouti, Z. Djouadi, N. Pinilla-Alonso, R. Brunetto, Near-infrared methanol bands probe energetic processing of icy outer solar system objects. *Astrophys. J.* **894**, L3 (2020).
49. R. G. Urso, V. Vuitton, G. Danger, L. Le Sergeant d'Hendecourt, L. Flandinet, Z. Djouadi, O. Mivumbi, F. R. Orthous-Daunay, A. Ruf, V. Vinogradoff, C. Wolters, R. Brunetto, Irradiation dose affects the composition of organic refractory materials in space. *Astron. Astrophys.* **644**, A115 (2020).
50. M. E. Brown, The compositions of Kuiper Belt objects. *Annu. Rev. Earth Planet. Sci.* **40**, 467–494 (2012).
51. M. A. Barucci, F. Merlin, A. Guilbert, C. de Bergh, A. Alvarez-Candal, O. Hainaut, A. Doressoundiram, C. Dumas, T. Owen, A. Coradini, Surface composition and temperature of the TNO Orcus. *Astron. Astrophys.* **479**, L13–L16 (2008).
52. W. M. Grundy, M. K. Bird, D. T. Britt, J. C. Cook, D. P. Cruikshank, C. J. A. Howett, S. Krijt, I. R. Linscott, C. B. Olkin, A. H. Parker, S. Protopapa, M. Ruaud, O. M. Umurhan, L. A. Young, C. M. Dalle Ore, J. J. Kavelaars, J. T. Keane, Y. J. Pendleton, S. B. Porter, F. Scipioni, J. R. Spencer, S. A. Stern, A. J. Verbiscer, H. A. Weaver, R. P. Binzel, M. W. Buie, B. J. Buratti, A. Cheng, A. M. Earle, H. A. Elliott, L. Gabasova, G. R. Gladstone, M. E. Hill, M. Horanyi, D. E. Jennings, A. W. Lunsford, D. J. McComas, W. B. McKinnon, R. L. McNutt, J. M. Moore, J. W. Parker, E. Quirico, D. C. Reuter, P. M. Schenk, B. Schmitt, M. R. Showalter, K. N. Singer, G. E. Weigle, A. M. Zangari, Color, composition, and thermal environment of Kuiper Belt object (486958) Arrokoth. *Science* **367**, eaay3705 (2020).
53. D. P. Cruikshank, Y. J. Pendleton, W. M. Grundy, Organic components of small bodies in the outer solar system: Some results of the *New Horizons* mission. *Life (Basel)* **10**, 126 (2020).
54. M. A. Barucci, M. E. Brown, J. P. Emery, F. Merlin, in *The Solar System Beyond Neptune*, M. A. Barucci, H. Boehnhardt, D. P. Cruikshank, A. Morbidelli, Eds. (University of Arizona Press, 2008), pp. 143–160.
55. I. Wong, M. E. Brown, A Hypothesis for the color bimodality of Jupiter Trojans. *Astron. J.* **152**, 90 (2016).
56. A. Ruf, A. Bouquet, P. Schmitt-Kopplin, P. Boduch, O. Mousis, G. Danger, Sulfur ion irradiation experiments simulating space weathering of Solar System body surfaces. *Astron. Astrophys.* **655**, A74 (2021).
57. A. Mahjoub, M. E. Brown, M. J. Poston, R. Hodyss, B. L. Ehlmann, J. Blacksberg, M. Choukroun, J. M. Eiler, K. P. Hand, Effect of H_2S on the near-infrared spectrum of irradiation residue and applications to the Kuiper Belt object (486958) Arrokoth. *Astrophys. J. Lett.* **914**, L31 (2021).

58. R. I. Kaiser, K. Roessler, Theoretical and laboratory studies on the interaction of cosmic-ray particles with interstellar ices. III. Suprathermal chemistry-induced formation of hydrocarbon molecules in solid methane (CH_4), ethylene (C_2H_4), and acetylene (C_2H_2). *Astrophys. J.* **503**, 959–975 (1998).
59. C. J. Bennett, C. P. Ennis, R. I. Kaiser, Implantation of energetic D^+ ions into carbon dioxide ices and implications for our solar system: Formation of D_2O and D_2CO_3. *Astrophys. J.* **794**, 57 (2014).
60. C. J. Bennett, C. Jamieson, A. M. Mebel, R. I. Kaiser, Untangling the formation of the cyclic carbon trioxide isomer in low temperature carbon dioxide ices. *Phys. Chem. Chem. Phys.* **6**, 735–746 (2004).
61. O. R. Hainaut, H. Boehnhardt, S. Protopapa, Colours of minor bodies in the outer solar system. *Astron. Astrophys.* **546**, A115 (2012).
62. O. R. Hainaut, A. C. Delsanti, Colors of minor bodies in the outer solar system. *Astron. Astrophys.* **389**, 641–664 (2002).
63. J. X. Luu, D. C. Jewitt, Charge-coupled device spectra of asteroids. I. Near-Earth and 3:1 resonance asteroids. *Astron. J.* **99**, 1985–2011 (1989).
64. J. Holmberg, C. Flynn, L. Portinari, The colours of the Sun. *Mon. Not. R. Astron. Soc.* **367**, 449–453 (2006).
65. N. Sakakibara, P. Y. Yu, T. Ito, K. Terashima, Cryogenic-specific reddish coloration by cryoplasma: New explanation for color diversity of outer solar system objects. *Astrophys. J.* **891**, L44 (2020).
66. Y. Y. Phua, N. Sakakibara, T. Ito, K. Terashima, Temperature-dependent kinetic analysis of cryogenic-specific reddish coloration synthesized with cryoplasma. *Icarus* **387**, 115152 (2022).
67. N. F. Kleimeier, Y. Liu, A. M. Turner, L. A. Young, C. H. Chin, T. Yang, X. He, J. I. Lo, B. M. Cheng, R. I. Kaiser, Excited state photochemically driven surface formation of benzene from acetylene ices on Pluto and in the outer solar system. *Phys. Chem. Chem. Phys.* **24**, 1424–1436 (2022).
68. W. M. Grundy, T. Bertrand, R. P. Binzel, M. W. Buie, B. J. Buratti, A. F. Cheng, J. C. Cook, D. P. Cruikshank, S. L. Devins, C. M. Dalle Ore, A. M. Earle, K. Ennico, F. Forget, P. Gao, G. R. Gladstone, C. J. A. Howett, D. E. Jennings, J. A. Kammer, T. R. Lauer, I. R. Linscott, C. M. Lisse, A. W. Lunsford, W. B. McKinnon, C. B. Olkin, A. H. Parker, S. Protopapa, E. Quirico, D. C. Reuter, B. Schmitt, K. N. Singer, J. A. Spencer, S. A. Stern, D. F. Strobel, M. E. Summers, H. A. Weaver, G. E. Weigle, M. L. Wong, E. F. Young, L. A. Young, X. Zhang, Pluto's haze as a surface material. *Icarus* **314**, 232–245 (2018).
69. V. A. Krasnopolsky, A photochemical model of Pluto's atmosphere and ionosphere. *Icarus* **335**, 113374 (2020).
70. M. L. Wong, S. Fan, P. Gao, M.-C. Liang, R.-L. Shia, Y. L. Yung, J. A. Kammer, M. E. Summers, G. R. Gladstone, L. A. Young, C. B. Olkin, K. Ennico, H. A. Weaver, S. A. Stern, The photochemistry of Pluto's atmosphere as illuminated by New Horizons. *Icarus* **287**, 110–115 (2017).
71. P. Lavvas, E. Lellouch, D. F. Strobel, M. A. Gurwell, A. F. Cheng, L. A. Young, G. R. Gladstone, A major ice component in Pluto's haze. *Nat. Astron.* **5**, 289–297 (2021).
72. S. G. Lias, J. E. Bartmess, J. F. Liebman, J. L. Holmes, R. D. Levin, W. G. Mallard, S. A. Kafafi, in *NIST Chemistry WebBook, NIST Standard Reference Database Number 69*, P. J. Linstrom, W. G. Mallard, Eds. (National Institute of Standards and Technology, 2018).
73. T. M. Halasinski, F. Salama, L. J. Allamandola, Investigation of the ultraviolet, visible, and near-infrared absorption spectra of hydrogenated polycyclic aromatic hydrocarbons and their cations. *Astrophys. J.* **628**, 555–566 (2005).
74. R. L. Hudson, R. F. Ferrante, M. H. Moore, Infrared spectra and optical constants of astronomical ices: I. Amorphous and crystalline acetylene. *Icarus* **228**, 276–287 (2014).
75. M. J. Abplanalp, R. I. Kaiser, Implications for extraterrestrial hydrocarbon chemistry: Analysis of acetylene (C_2H_2) and D2-acetylene (C_2D_2) ices exposed to ionizing radiation via ultraviolet–visible spectroscopy, infrared spectroscopy, and reflectron time-of-flight mass spectrometry. *Astrophys. J.* **889**, 3 (2020).
76. G. Socrates, Ed. *Infrared and Raman Characteristic Group Frequencies: Tables and Charts* (Wiley, 2004).
77. R. L. Hudson, Y. Y. Yarnall, Infrared spectra and optical constants of astronomical ices: IV. Benzene and pyridine. *Icarus* **377**, 114899 (2022).
78. M. J. Abplanalp, B. M. Jones, R. I. Kaiser, Untangling the methane chemistry in interstellar and solar system ices toward ionizing radiation: A combined infrared and reflectron time-of-flight analysis. *Phys. Chem. Chem. Phys.* **20**, 5435–5468 (2018).
79. R. I. Kaiser, K. Roessler, Theoretical and laboratory studies on the interaction of cosmic-ray particles with interstellar ices. I. Synthesis of polycyclic aromatic hydrocarbons by a cosmic-ray-induced multicenter mechanism. *Astrophys. J.* **475**, 144–154 (1997).
80. C. J. Bennett, C. S. Jamieson, Y. Osamura, R. I. Kaiser, Laboratory studies on the irradiation of methane in interstellar, cometary, and solar system ices. *Astrophys. J.* **653**, 792–811 (2006).
81. R. I. Kaiser, N. Hansen, An aromatic universe—A physical chemistry perspective. *J. Phys. Chem. A* **125**, 3826–3840 (2021).
82. A. G. G. M. Tielens, Interstellar polycyclic aromatic hydrocarbon molecules. *Annu. Rev. Astron. Astrophys.* **46**, 289–337 (2008).
83. T. Stephan, TOF-SIMS in cosmochemistry. *Planet. Space Sci.* **49**, 859–906 (2001).
84. T. Stephan, E. Jessberger, C. Heiss, D. Rost, TOF-SIMS analysis of polycyclic aromatic hydrocarbons in Allan Hills 84001. *Meteorit. Planet. Sci.* **38**, 109–116 (2002).
85. R. Luna, M. Á. Satorre, M. Domingo, C. Millán, C. Santonja, Density and refractive index of binary CH_4, N_2 and CO_2 ice mixtures. *Icarus* **221**, 186–191 (2012).
86. A. M. Turner, M. J. Abplanalp, S. Y. Chen, Y. T. Chen, A. H. Chang, R. I. Kaiser, A photoionization mass spectroscopic study on the formation of phosphanes in low temperature phosphine ices. *Phys. Chem. Chem. Phys.* **17**, 27281–27291 (2015).
87. G. Tarczay, M. Forstel, P. Maksyutenko, R. I. Kaiser, Formation of higher silanes in low-temperature silane (SiH_4) ices. *Inorg. Chem.* **55**, 8776–8785 (2016).
88. P. A. Gerakines, R. L. Hudson, Infrared spectra and optical constants of elusive amorphous methane. *Astrophys. J.* **805**, L20 (2015).
89. P. B. Crandall, J. J. Gillis-Davis, R. I. Kaiser, Untangling the origin of molecular hydrogen in the lunar exosphere. *Astrophys. J.* **887**, 27 (2019).
90. H. Van Den Dool, P. D. Kratz, A generalization of the retention index system including linear temperature programmed gas–liquid partition chromatography. *J. Chromatogr. A* **11**, 463–471 (1963).
91. M. L. Lee, D. L. Vassilaros, C. M. White, Retention indices for programmed-temperature capillary-column gas chromatography of polycyclic aromatic hydrocarbons. *Anal. Chem.* **51**, 768–773 (1979).
92. V. I. Babushok, P. J. Linstrom, On the relationship between Kováts and Lee Retention indices. *Chromatographia* **60**, 725–728 (2004).

Acknowledgments

Funding: This study was supported by the U.S. National Aeronautics and Space Administration (NASA) under grant no. 80NSSC21K1834 and the European Union Framework Program for Research and Innovation HORIZON 2020 under grant ERC 804144. **Author contributions:** R.I.K. designed the experiments. C. Zhang, C. Zhu, A.M.T., and I.O.A. performed experiments, A.D.G. and C.M. performed the gas chromatographic analyses. All authors discussed the data. The manuscript was read, revised, and approved by all coauthors. **Competing interests:** The authors declare that they have no competing interests. **Data and materials availability:** All data needed to evaluate the conclusions in the paper are present in the paper and/or the Supplementary Materials.

Submitted 14 January 2023
Accepted 21 April 2023
Published 31 May 2023
10.1126/sciadv.adg6936

ScienceAdvances

Processing of methane and acetylene ices by galactic cosmic rays and implications to the color diversity of Kuiper Belt objects

Chaojiang Zhang, Cheng Zhu, Andrew M. Turner, Ivan O. Antonov, Adrien D. Garcia, Cornelia Meinert, Leslie A. Young, David C. Jewitt, and Ralf I. Kaiser

Sci. Adv., **9** (22), eadg6936.
DOI: 10.1126/sciadv.adg6936

Science Advances (ISSN) is published by the American Association for the Advancement of Science. 1200 New York Avenue NW, Washington, DC 20005. The title *Science Advances* is a registered trademark of AAAS.